# LWS BEAM PROFILE

The mean beam profile is derived from a series of standard bias, grating scan observations of Mars. One observation was made on axis and the others were distributed around the field as shown in Figure 1. The mean flux in each detector at each of the raster positions is used to describe the radial sensitivity of the instrument and a parameterisation defines the mean beam profile. In addition subsets of the data along the four radial alignments, which are labelled PA30, PA75, PA120 and PA165 on Figure 1, have been analyzed to investigate possible asymmetries in the beam profile.

The optical train of the LWS consist of the CFM that allows a beam of $\sim$ 120 arcsec to fall on the mirror M2 which is inclined at $\sim$ 22 degrees to the incoming beam. M2 then presents an elliptical beam of $\sim 105 \times 97$ arcsec (nominal FWHM) to the collimator, the LWS entrance pupil and the re-imaging mirror. Projected onto the sky the long and short axes of M2 are PA30 and PA120 (Y and Z axes) respectively.

The mean beam profiles were calculated using only the points with r $< 65$ arcsec, although the point on axis was also excluded. These points lie on the 'active' part of the profile and provide the best constraint of the width of the profile. The central point was used to normalise the fluxes, so they are all relative to the on-axis value in each detector, although this was not always the highest flux. For simplicity a Gaussian profile has been fitted, and it has been constrained to be symmetrical about the optical axis. The data are sufficiently

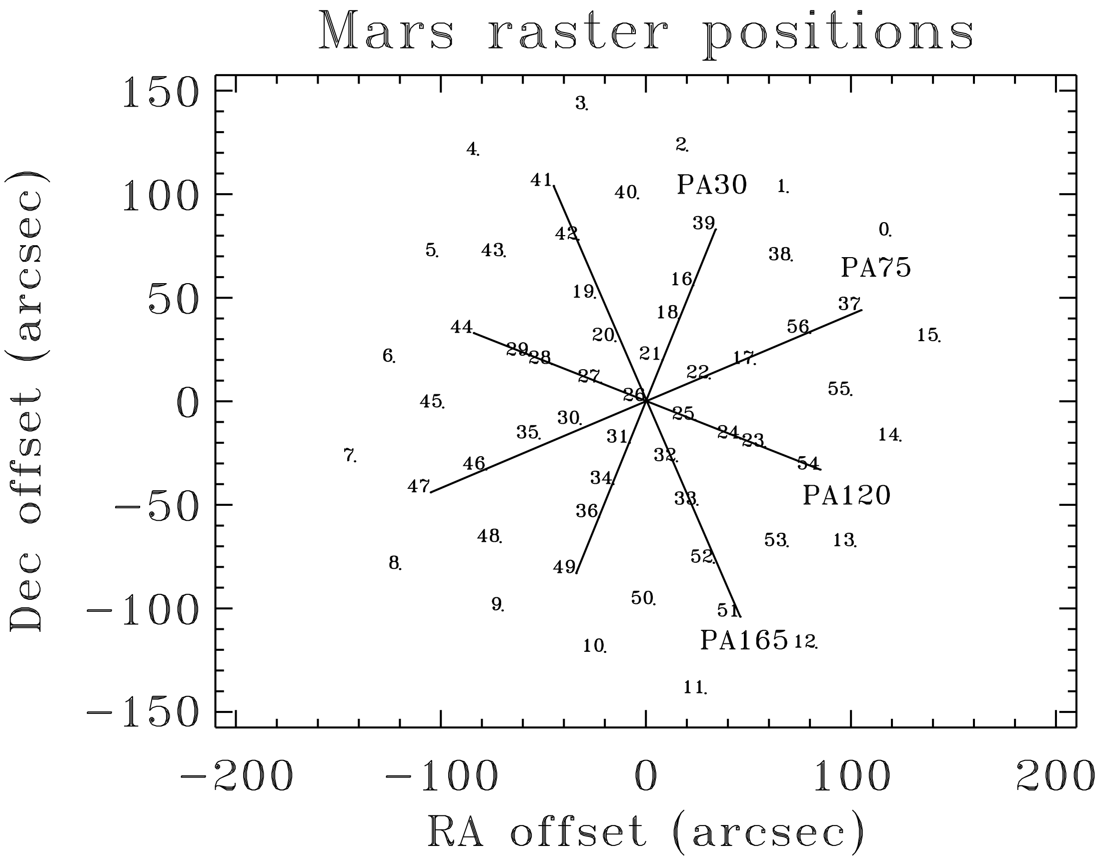


Figure 1: Mars data raster positions

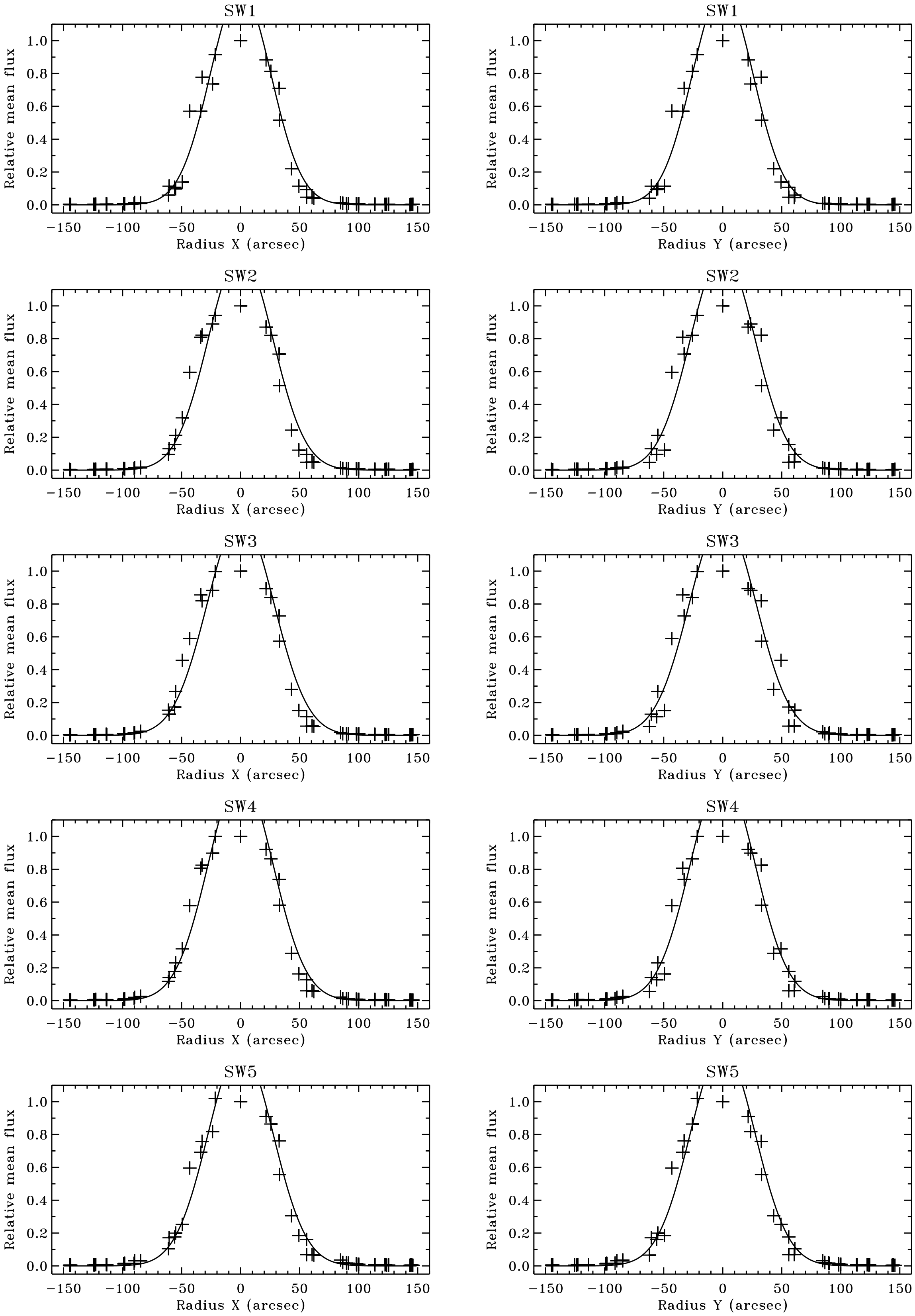


Figure 2: All data SW detectors

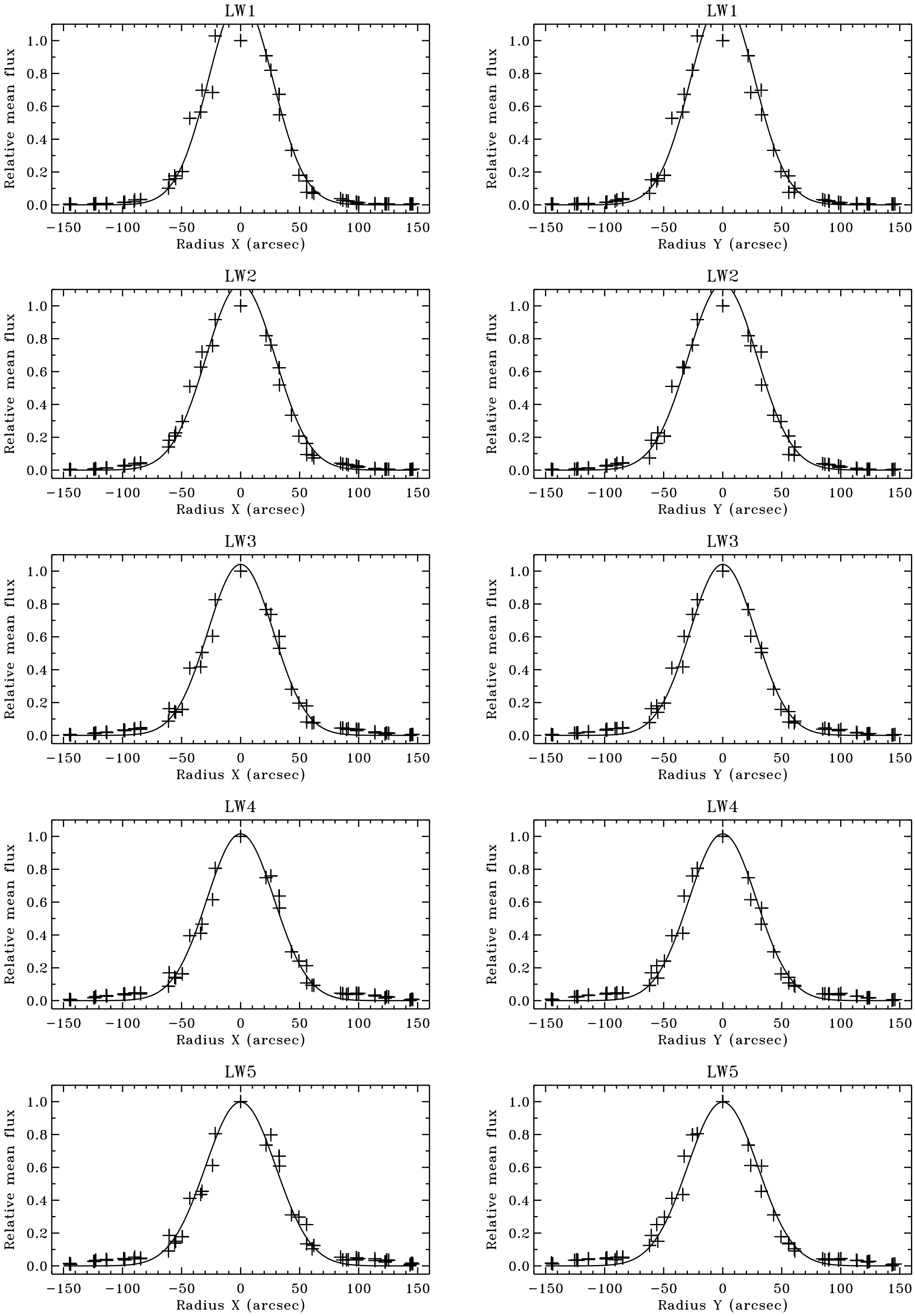


Figure 3: All data LW detectors

noisy, or perhaps inconsistent, that the true form of the profile is not clear. These fits are generally better, ie. more Gaussian, than those that included all the points out into the wings, although in practice there is only a small difference in the parameters of the fit. The points in the wings are clearly not Gaussian and one consequence of this is that for the LW detectors, in particular LW5, the fitted profile appears too weak at large radii. It has been recognised for some time that the out-lying points are bright, possibly due to sky contamination or scattered light. Fitting this background rather better will make very little difference to the parameters of core of the profile.

The profile fits are shown in Figures 2 and 3. For each detector the relative flux is plotted against radius with the sign taken from the X and Y offset respectively for the two cases (Radius X, Radius Y). This allows any distortions in each quadrant to be seen. It is clear that the Gaussian profile is a reasonable fit to the data, except for the point on axis. For the SW detectors, and to a lesser extent the LW detectors, the flux on axis is low relative to the profile, indicating that the detector response is flattened near the centre. The precise shape of this region is impossible to determine but in the absence of any other guidance it will be assumed to be flat. Optical modelling also predicts a plateau with a slightly raised rim (Swinyard, Beam Working Group Report No.1, Caldwell et al. Beam clipping report.).

In most of the plots three regions can be identified; (i) a central plateau, (ii) a Gaussian-like profile, and (iii) the extended wings. The width of the plateau is almost constant for the SW detectors but decreases dramatically for the LW detectors. For LW3 is the plateau is marginal and it vanishes for LW4 and LW5. In most cases the symmetric Gaussian profile is a good fit to the mean radial distribution but in some cases, particularly for SW2, SW3 and SW4, groups of points tend to lie systematically towards negative X and, to a lesser extent, negative Y. In contrast, the LW detectors are well fitted by a Gaussian profile with little evidence of any systematic errors. Finally, the extended wings are well fitted, compared to the other errors, for all the SW detectors although there is an increasing systematic trend for the points to lie above the profile, which increases in the LW detectors. By LW3 the difference is quite noticeable and the errors approach those in the rest of the profile.

In Table 1 the measured values of the relevant parameters of the fit are given. The FWHM is the full width of the profile at a relative intensity, I = 0.5 with respect to the central (on-axis) value. The PLATEAU value is the radius of the central region where the relative intensity, I = 1.0 by definition. The parameters A and SIGMA define the profile at radius, R > PLATEAU.

So at R < PLATEAU, I = 1.0

at R > PLATEAU, $I = A \exp(-0.5(R/SIGMA)^2)$

The parameter FWHM' is the full width of the profile that contains half the flux, which is identical to the FWHM for a purely Gaussian profile. Finally the parameter R is the effective radius of a cylindrical profile containing the same flux as the observed profile. The conversion to flux/steradian is through the relationship

flux/steradian = flux/(2.PI(1-cos(R.PI/648000.0)))

where R is the effective radius in Table 1.

Each of the radial alignments is a subset of the data used to calculate the global mean profiles. The four alignments are separated by approximately 45 degrees to create two

Table 1: BEAM PROFILE TABLE V3.0

| Detector | FWHM | PLATEAU | A | SIGMA | R | FWHM' |
|---|---|---|---|---|---|---|
| SW1 | 71.7 | 18.8 | 1.3028 | 25.9 | 41.2 | 62.3 |
| SW2 | 76.3 | 20.3 | 1.3165 | 27.4 | 43.8 | 66.1 |
| SW3 | 79.2 | 21.1 | 1.3149 | 28.5 | 45.5 | 68.6 |
| SW4 | 78.4 | 21.7 | 1.3607 | 27.7 | 44.8 | 67.0 |
| SW5 | 77.3 | 20.6 | 1.3173 | 27.8 | 44.3 | 66.8 |
| LW1 | 74.1 | 18.5 | 1.2586 | 27.3 | 42.7 | 65.2 |
| LW2 | 75.0 | 14.6 | 1.1326 | 29.3 | 44.0 | 69.4 |
| LW3 | 67.3 | 7.9 | 1.0414 | 27.8 | 40.1 | 65.4 |
| LW4 | 68.0 | 5.0 | 1.0157 | 28.6 | 40.7 | 67.3 |
| LW5 | 70.0 | 0.0 | 1.0000 | 29.7 | 42.0 | 70.0 |

orthogonal pairs, with the PA30 set aligned along the Y axis, and the PA120 set aligned along the Z axis of M2. Each of these alignments contains nine points but the radial distribution of the alternate pairs is rather different. The Gaussian profile was fitted in the same way as with the complete data set, with the on-axis point excluded, and using only the points with $r < 65$ arc seconds. The main concern with this process is the poor statistics. Although each alignment contains nine points, only six points are used in the PA30 and PA120 solutions and only four points in the PA75 and PA165 solutions. Despite these limitations the fits show the same features as the global solutions. The point on axis is low compared to the profiles and the distribution becomes more Gaussian towards longer wavelengths. The fits to all the detectors for each alignment are shown in Figures 4 to 7. The plots show the relative mean flux against radius with the sign from the X offset. On the PA30 alignment all the detectors show some degree of asymmetry towards negative X. While this is marginal for the LW detectors it is very consistent and there is also a clear distortion of the distribution at X=-45 which increases towards shorter wavelengths. The distribution for PA75 is less clear with the SW detectors showing some degree of asymmetry towards negative X and the LW detectors towards positive X. The LW distribution at PA120 is similar to that at PA75 while the SW distribution is generally symmetric apart from the discordant points at X=-50. Finally, the PA165 distribution is the most symmetric apart from a slight tendency towards positive X for the longer wavelength LW detectors.

Of the parameters derived from these solutions the FWHM are probably the most reliable, and these are shown in Figure 8. Although there is considerable scatter the behaviour is fairly consistent. Each alignment shows an increase in FWHM through the SW detectors and then a subsequent decline, which reflects the behaviour of the global FWHM values. In more detail it can be seen that the alignments fall naturally into two pairs with very similar behaviour. PA75 and PA120 show much more variation than PA30 and PA165, and peak at SW3 as opposed to SW5. All four alignments show the little feature at LW2 and an increase in FWHM from LW3 to LW5. It might be expected that the variation is in some way symmetrical with respect to the axis of M2. The alignments PA30 and PA120 are the orthogonal axes of M2 and might be expected to show the extreme values. PA120 certainly has the narrowest widths, and is systematically smaller than PA30 but the intermediate alignments PA75 and PA165 show a similar level of disagreement. The mean ratio of the Y and Z axis FWHM is 0.93 which is remarkably, if not reassuringly, similar to the expected ratio of the ellipticity of the beam from M2, ie. 0.93. The level of agreement with the predicted value must be a little fortuitous given the scatter in the measurements, but the unresolved problem remains the size of the beam which is $\sim 75\%$ of that expected. To what extent clipping of the Airy profile by M2 and LWS entrance pupil is responsible is not yet

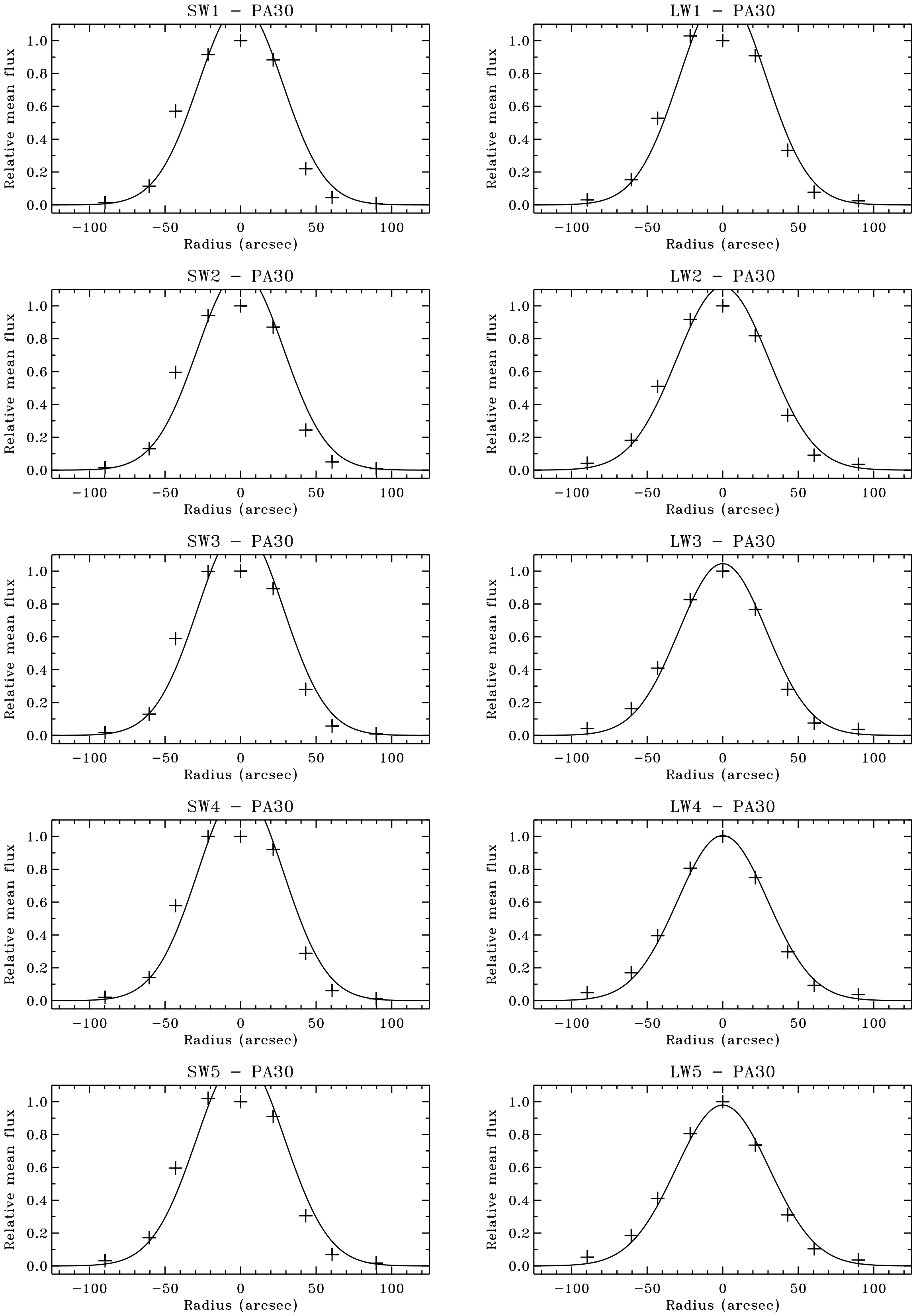


Figure 4: PA30

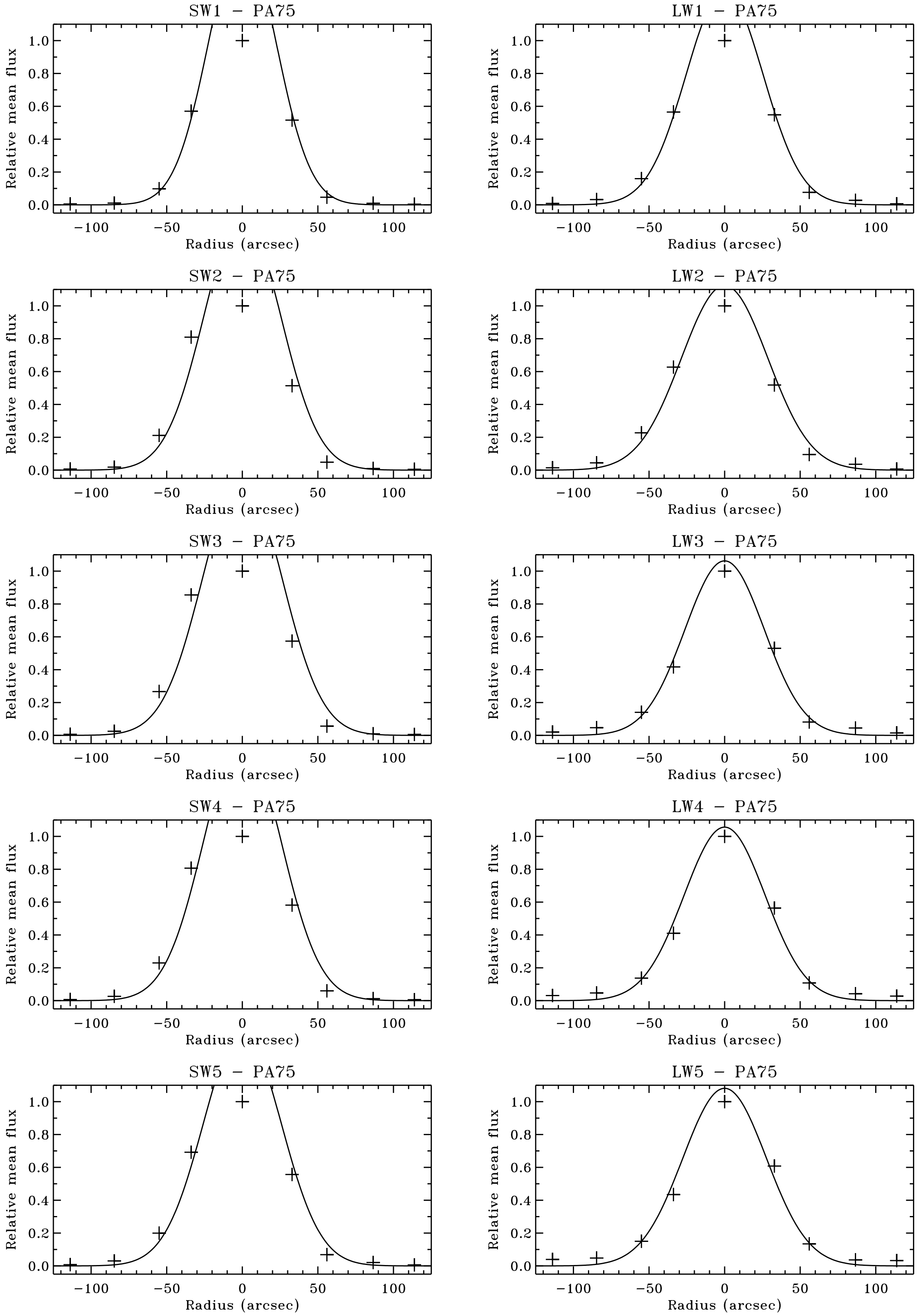


Figure 5: PA75

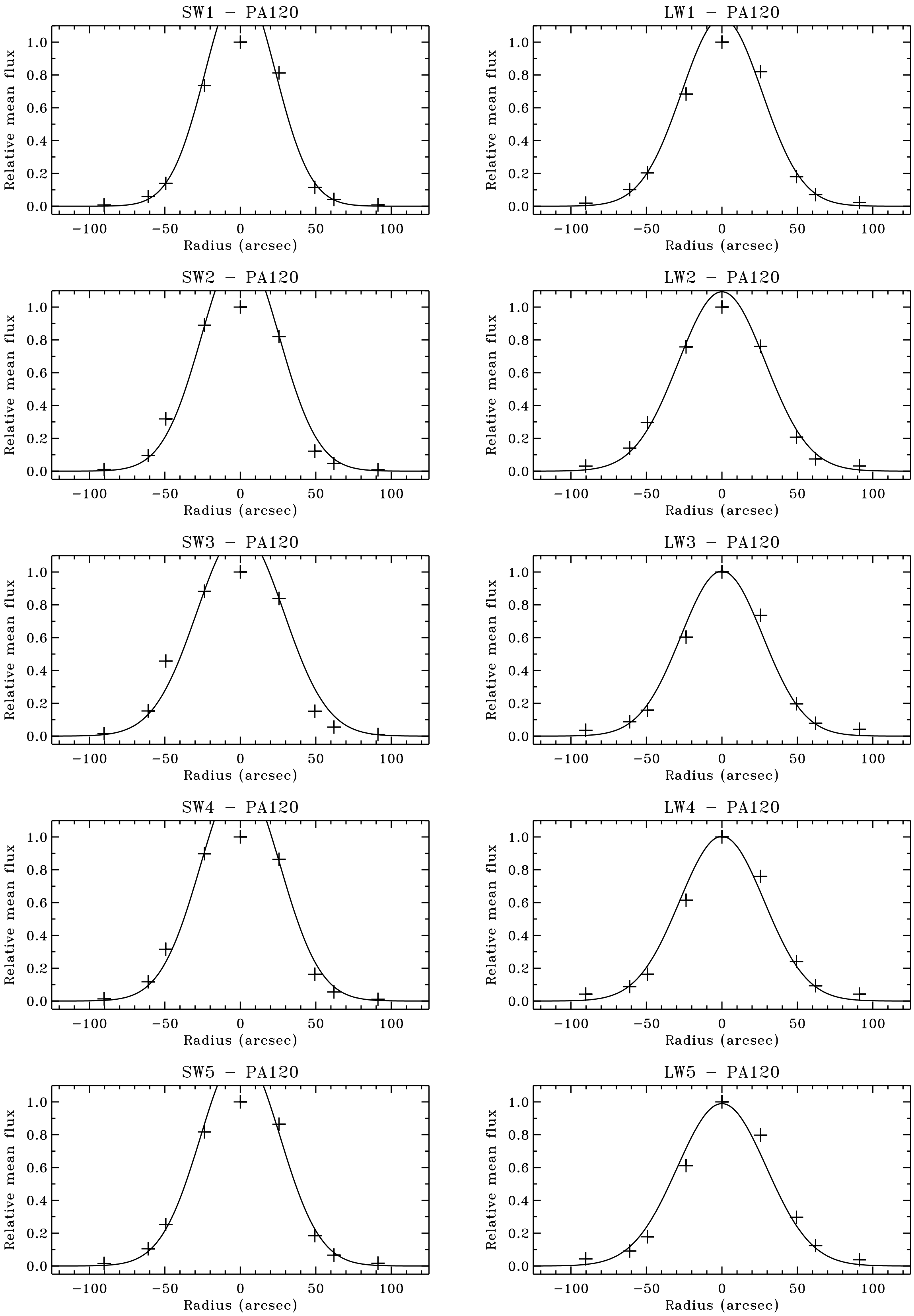


Figure 6: PA120

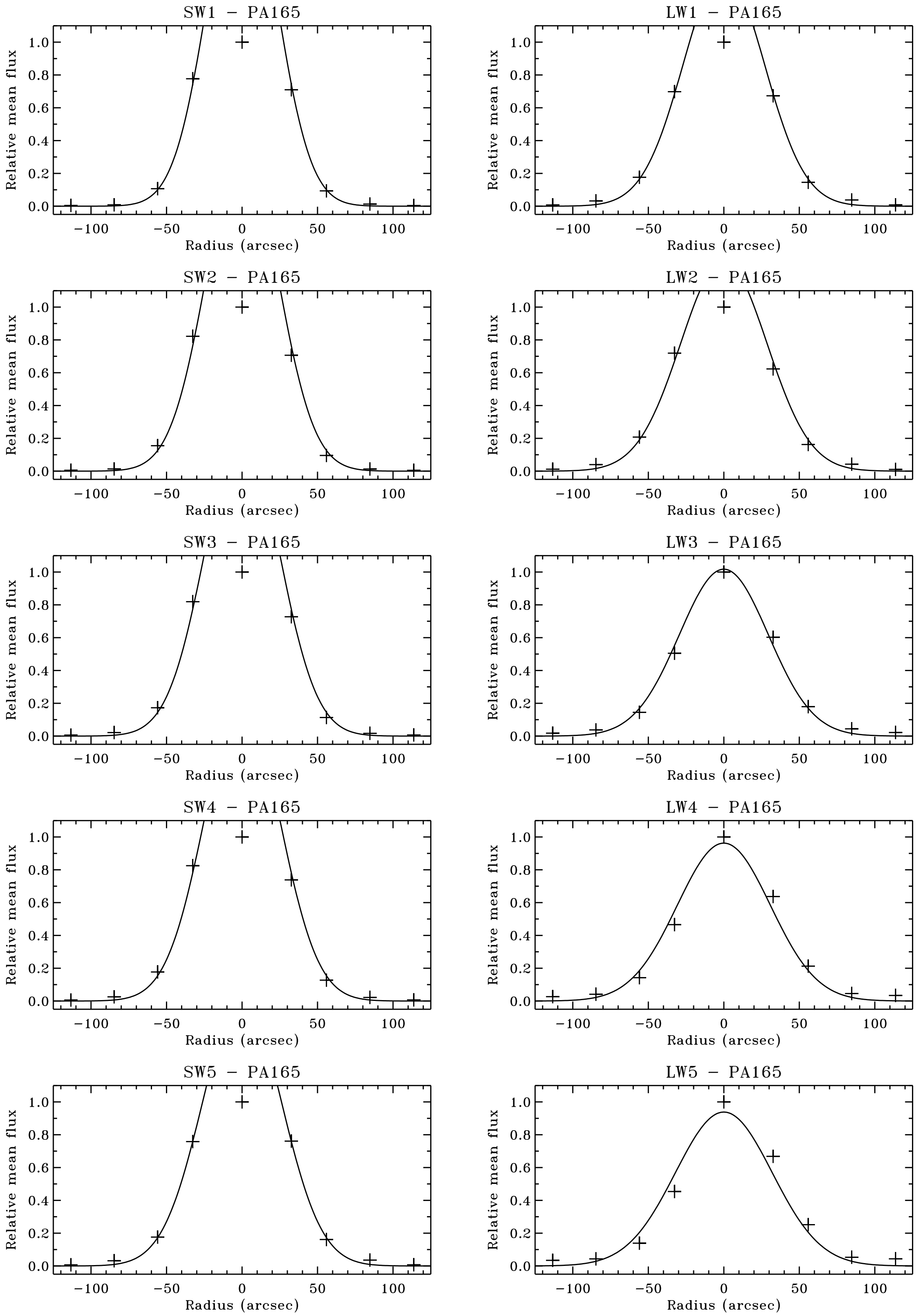


Figure 7: PA165

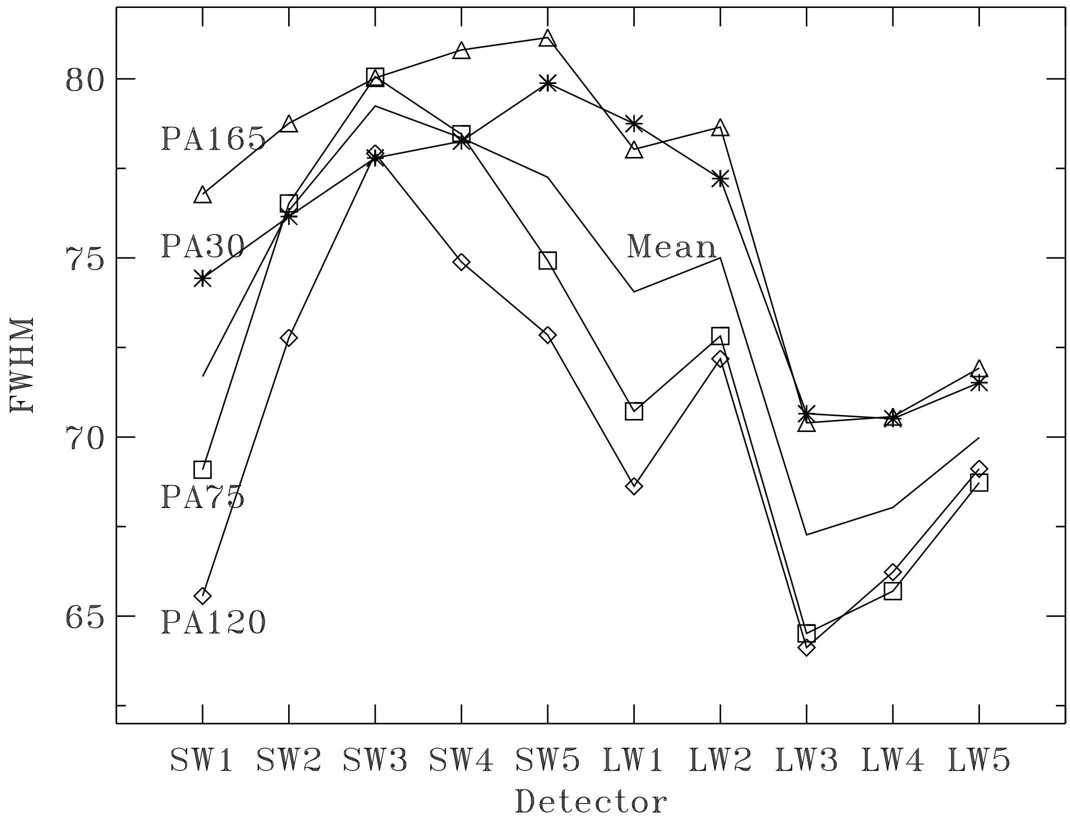


Figure 8: FWHM vs. detector for the four alignments

clear (Swinyard, Beam Working Group Report No.1, Caldwell et al. Beam clipping report.).

The mean fluxes conceal a wide range of variation with wavelength at each of the raster positions and it is likely that some of the explanation for the behaviour in Figure 8 will be found here. Figure 9 shows the flux relative to the on-axis value at each wavelength across all detectors at the inner four raster positions on each alignment. In general the agreement between detectors (stitching) is good and for the positions closest to the axis the relative flux is fairly constant. With increasing radius the relative flux becomes less constant and the fringing becomes more visible. However, in one sector, the negative X offset (Figure 1) between PA75 and PA120, the relative fluxes show a very different, fractured pattern (positions 27, 28, 30 and 35). The same effect may also be weakly visible on PA165 (positions 19 and 20) but does not appear to affect PA30 (positions 31 and 34). The origin of this fractured pattern in the fluxes is presently unknown but vignetting in the beam from M2 is suspected.

The relative fluxes at the eight positions on the inner ring are shown in more detail in Figure 10. By a radius of 90 arcsec the behaviour of the fluxes in the LW detectors are relatively similar across the whole field but in the affected sector the SW detectors still show the fractured pattern (Figure 11).

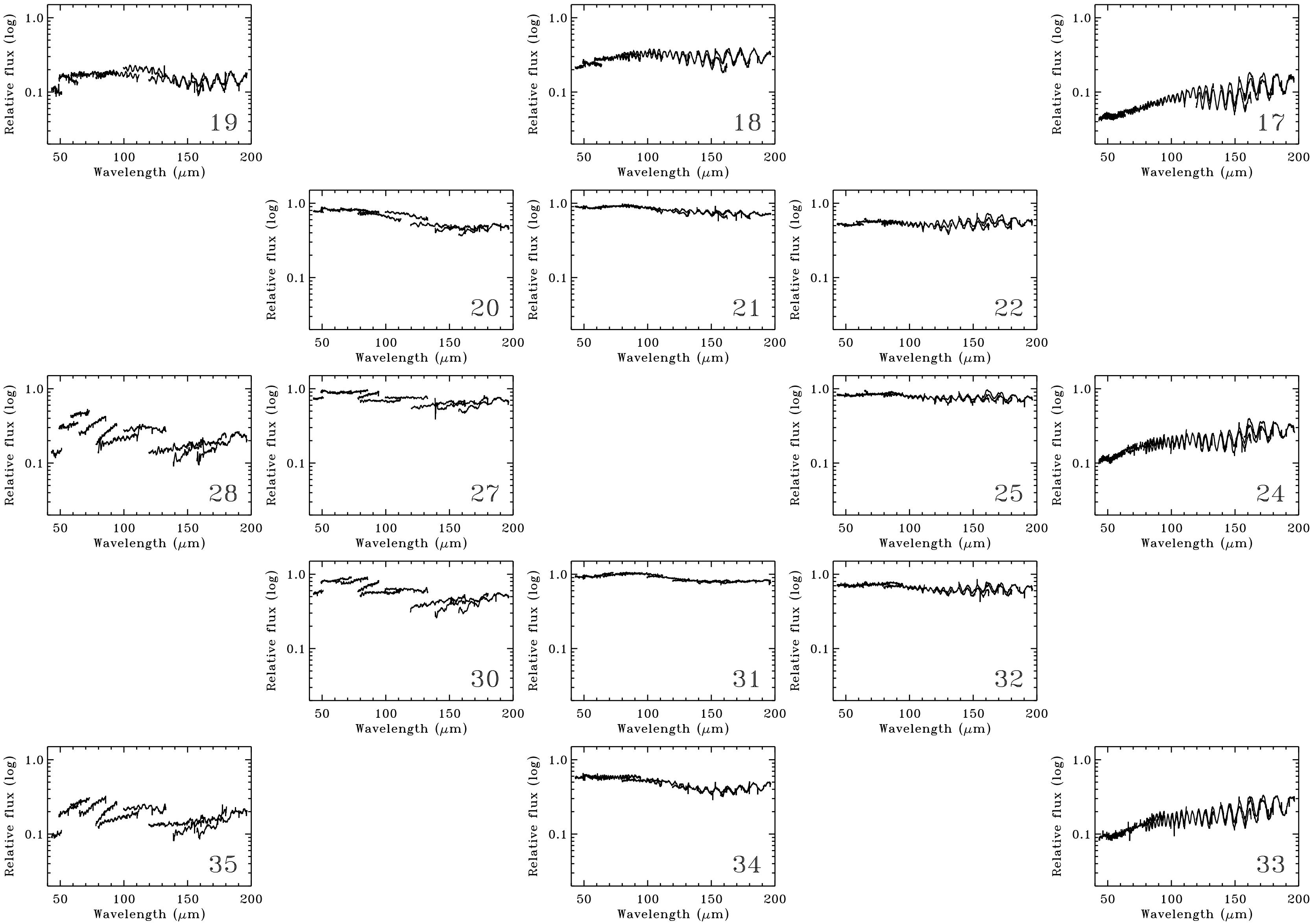


Figure 9: Relative fluxes for the inner region. In this plot PA30 is vertical.

The fringing that appears at positions off axis is believed to be due to interference between the direct beam from M2 and the reflection from the substrate supporting M2. The prediction from the model, such as it is, suggest that the phasing of the fringing should remain constant. The relative fringe amplitude should increase with radius until the maximum amount of the beam is reflected from the substrate, at $r \sim 60$ arcsec, then decline as the beam moves off the substrate, and then show a secondary maximum where the first Airy ring illuminates the substrate.

Figure 12 shows the relative flux in the LW detectors at three positions on PA30 and PA120, all at a radius of 61 arcsec. Two of the positions, 16 and 36, are opposite and 23 is orthogonal. For positions 16 and 23 it is immediately clear that the fringe phasing is not constant and between positions 16 and 36 the phasing seems to change with wavelength. The fringe amplitude is clearly a function of wavelength. There is also some difference in the fringe amplitude at the same radius and this is seen more clearly in Figure 13, which shows the fluxes at another trio of positions at a radius of 55 arcsec from PA75 and PA165.

An illustration of the radial distribution of the fringe amplitude is given in Figure 14 which shows the relative fluxes in LW4 at positions on and between PA75 and PA120 (positive X offset). The amplitude increases steadily to $r \sim 60$ arcsec but practically vanishes by $r \sim 90$ arcsec only to show a slight increase again by the edge of the field, as predicted by the model. The fluxes at eight positions around the edge of the field are shown in Figure 15, and show considerable variation in the fringe visibility.

In order to parameterise the fringe phase and amplitude behaviour across the instrument it is necessary to fit and determine the fringe pattern. Figure 16 is simply to illustrate some of the difficulties of this process. The spectrum contains features that will confuse the fit and the model does not always appear to adequately fit the fringing. The relative fringe amplitude and the relative flux can change significantly across one detector which undermines a simple parameterisation.

Future developments will include a parameterisation of the fringe phase and amplitude, and a revised mean beam profile corrected for fringing and the inclusion of some correction for the increasing background in the LW detectors.

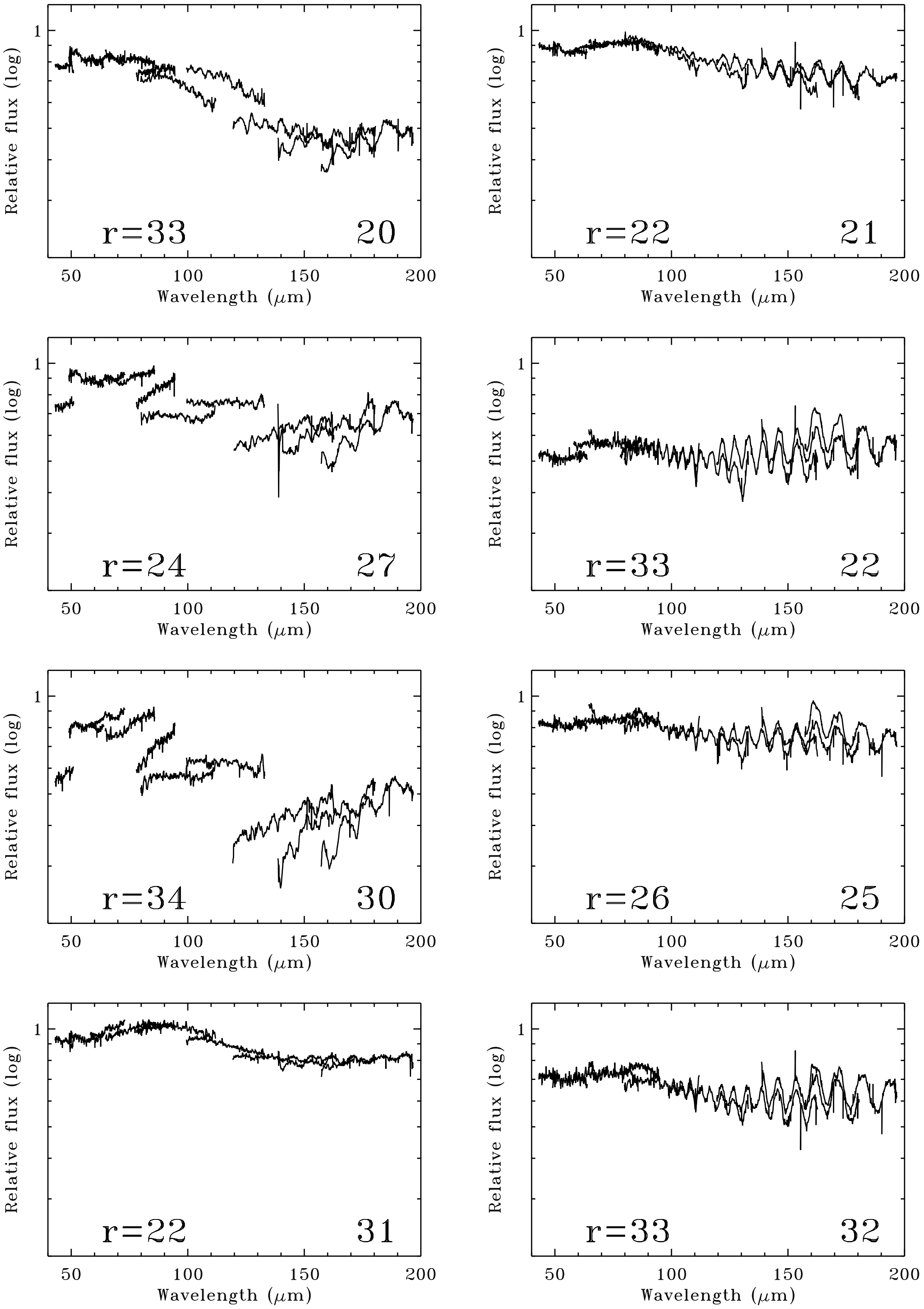


Figure 10: Inner ring

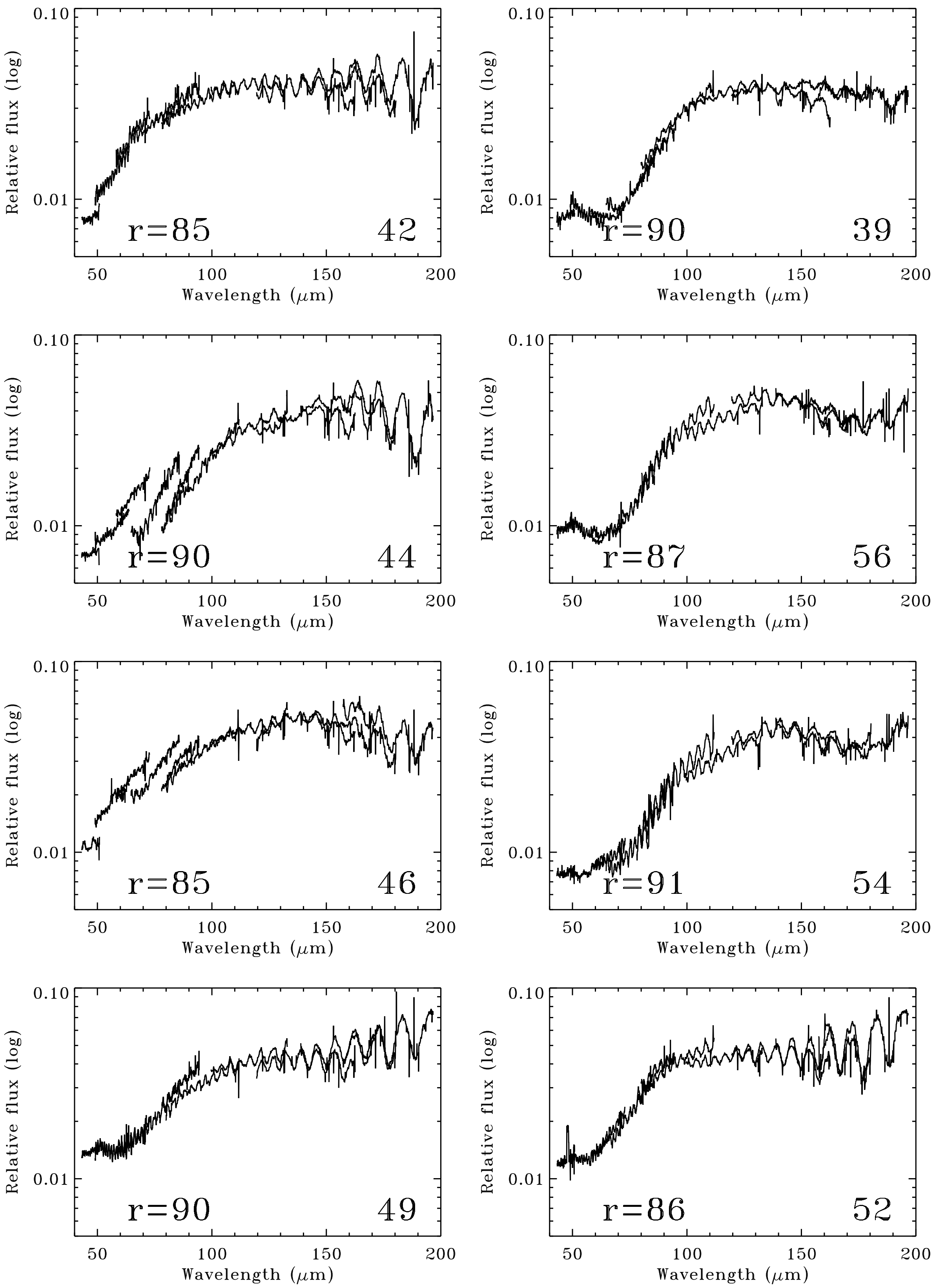


Figure 11: Intermediate ring

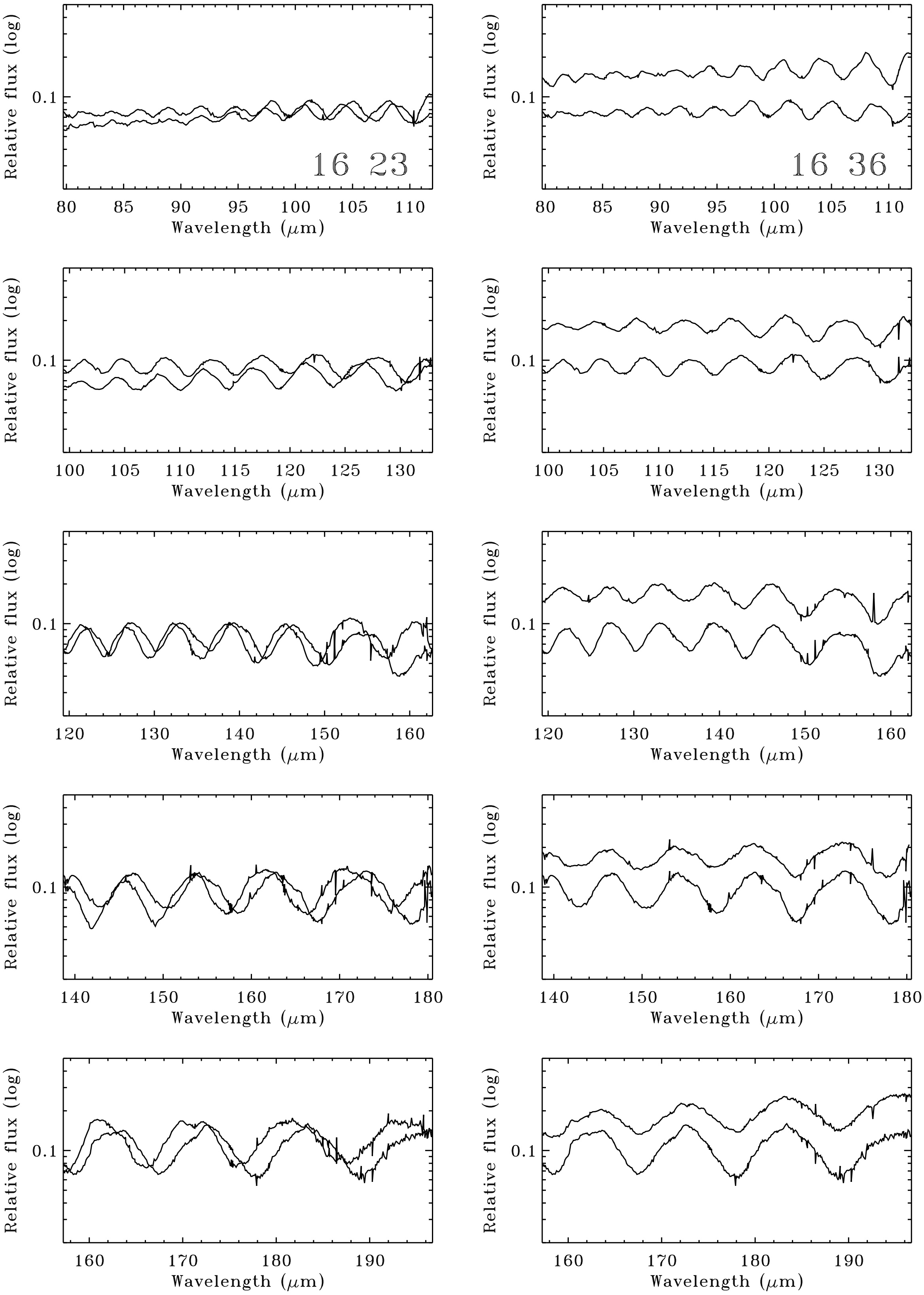


Figure 12: Opposite and orthogonal pairs on PA30 and PA120 at 61 arcsec.

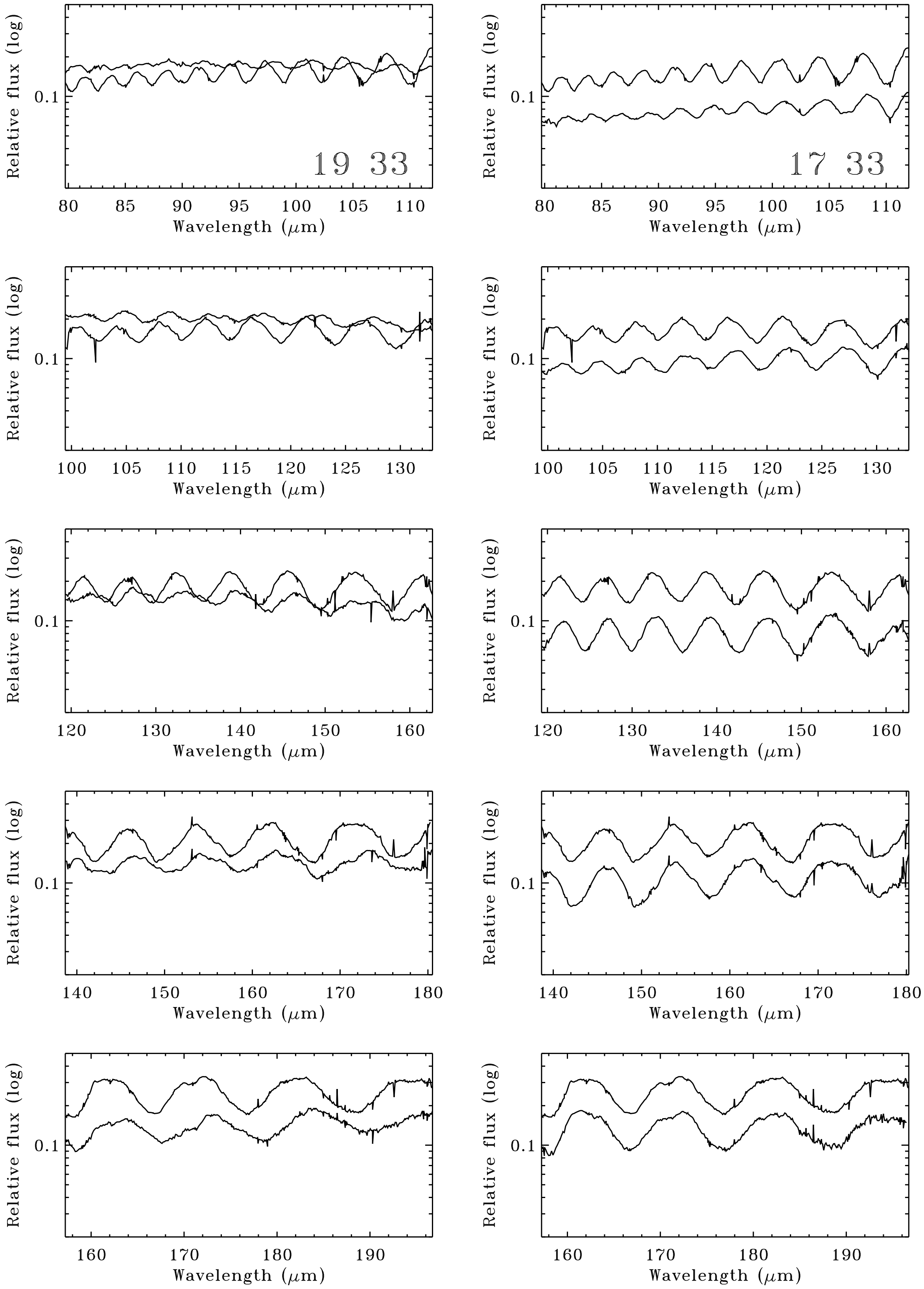


Figure 13: Opposite and orthogonal pairs on PA75 and PA120 at 55 arcsec.

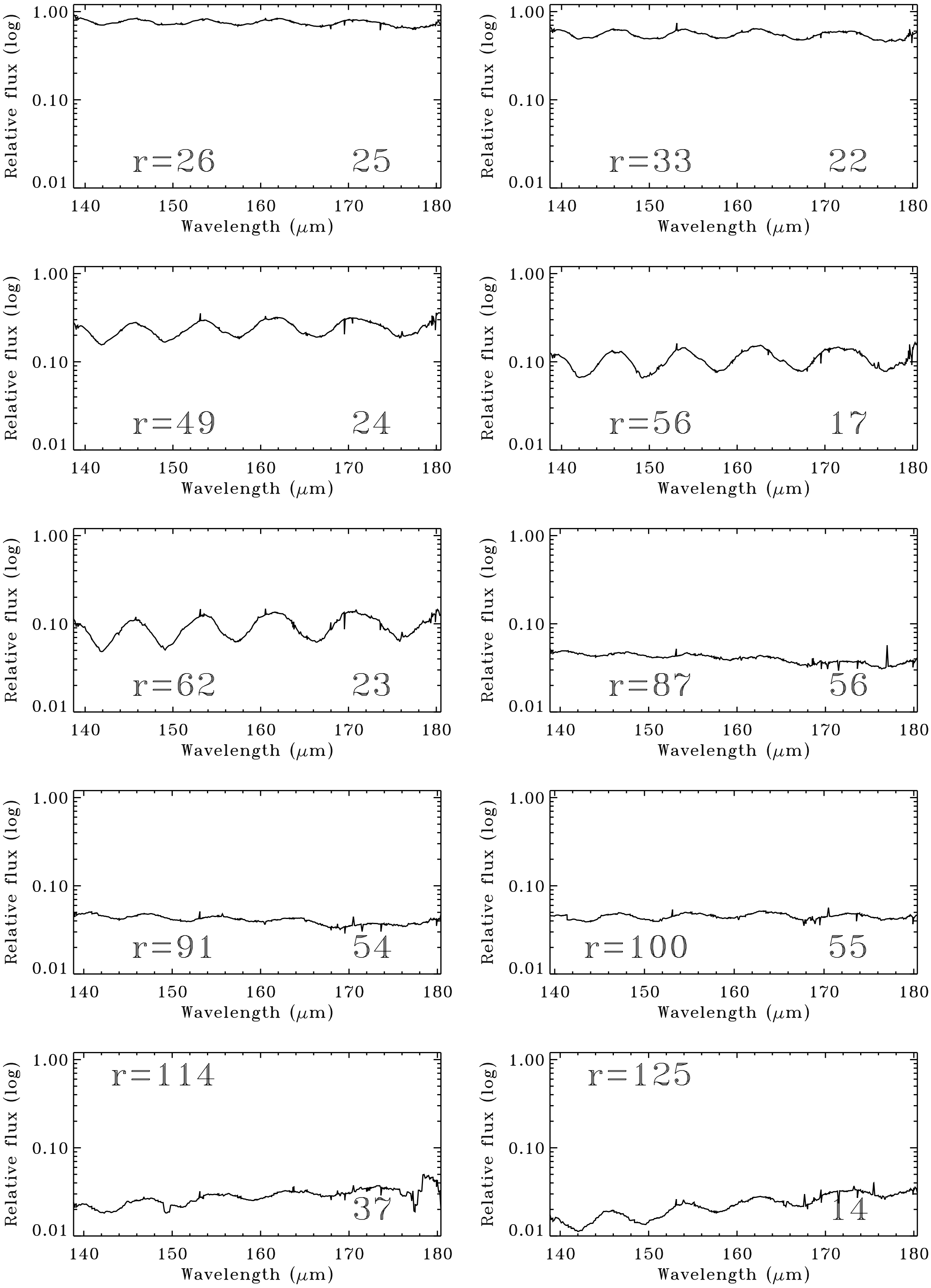


Figure 14: Radial progression of the fringe amplitude

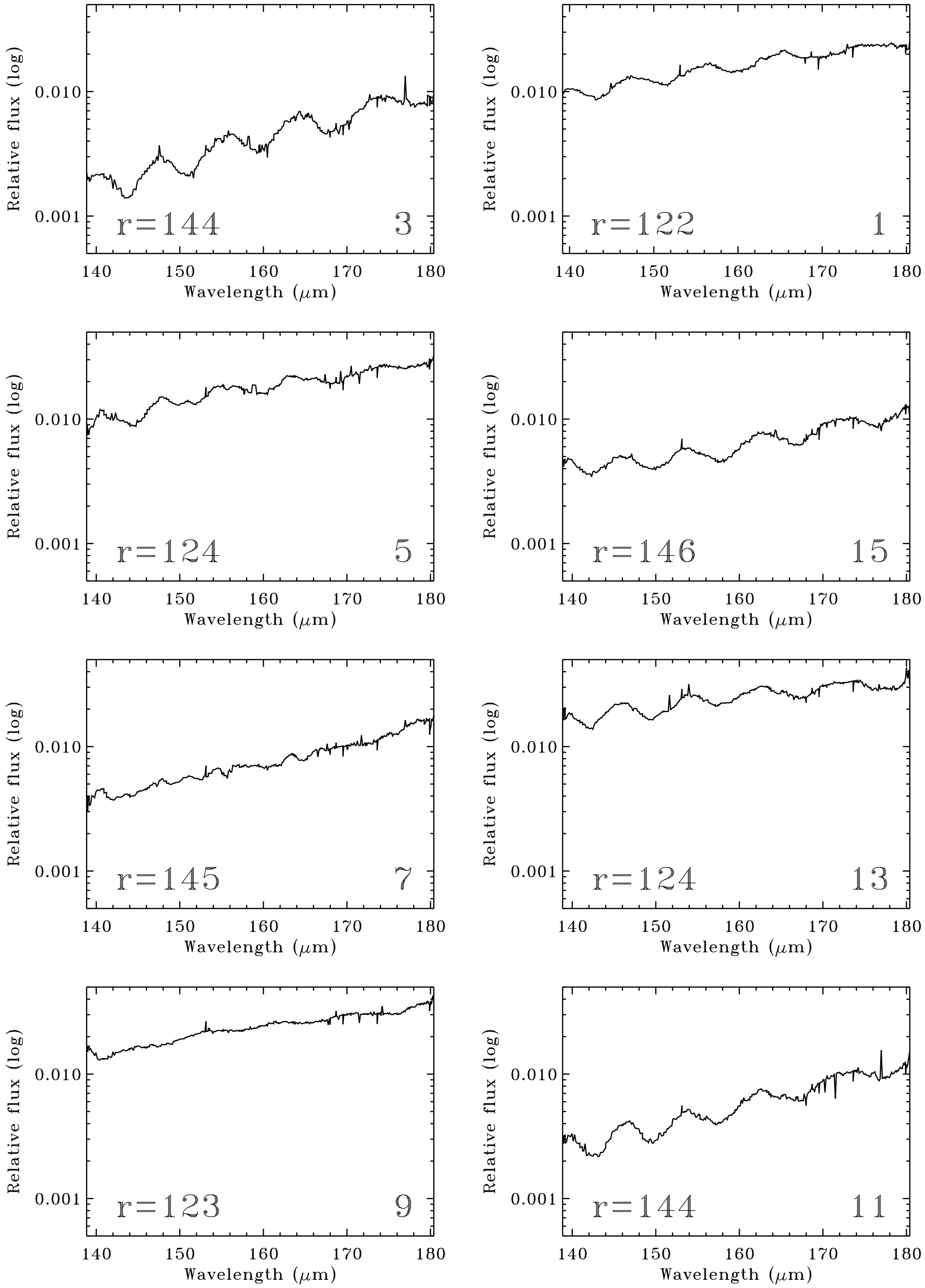


Figure 15: Alternate positions on outer edge.

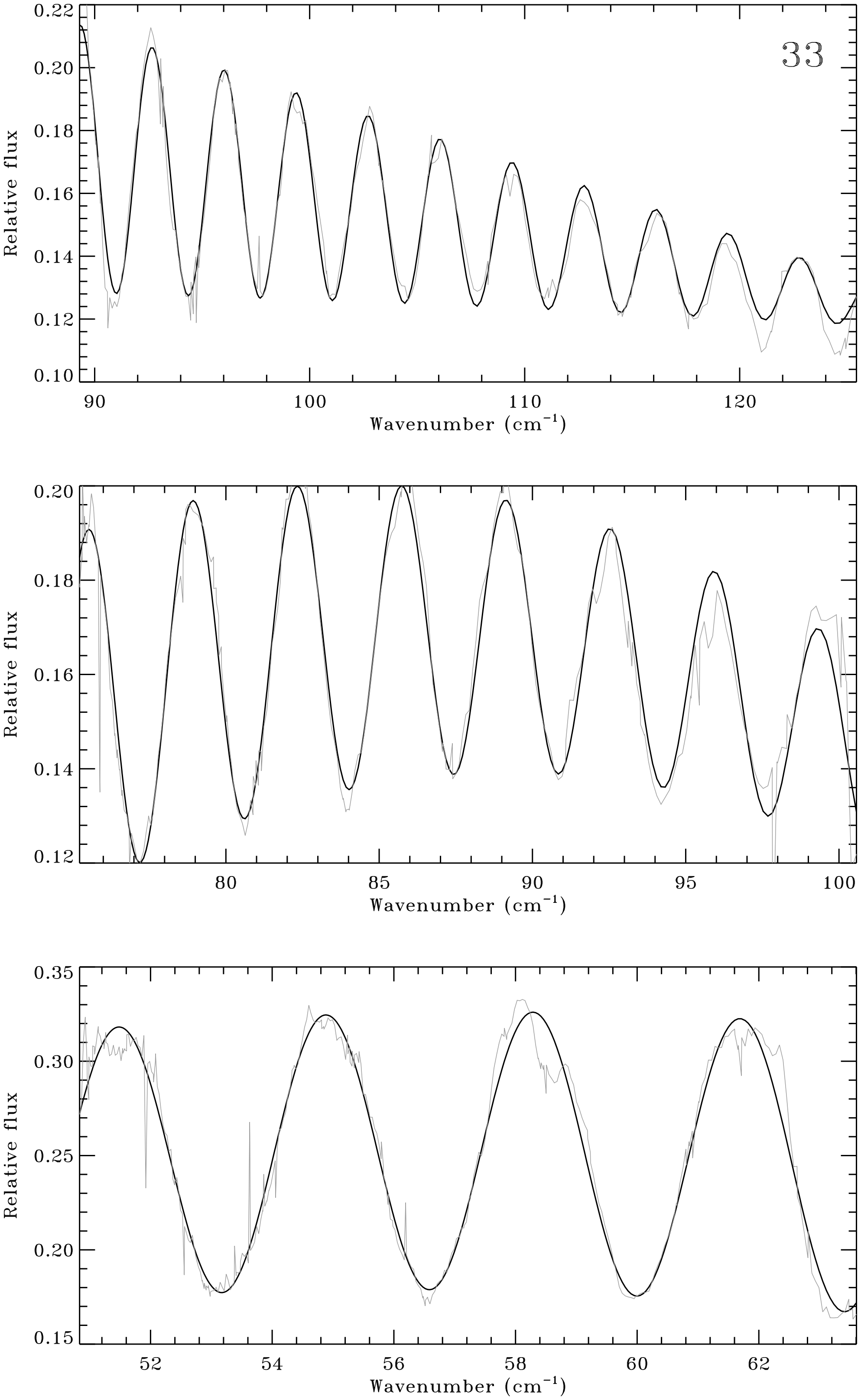


Figure 16: Relative fringe patterns for LW1, LW4 and LW5 at position 33.